Hypersonic and Supersonic Static Aerodynamics of Mars Science Laboratory Entry Vehicle

Artem A. Dyakonov[*], Mark Schoenenberger[†] and John W. Van Norman[‡]

This paper describes the analysis of continuum static aerodynamics of Mars Science Laboratory (MSL) entry vehicle (EV). The method is derived from earlier work for Mars Exploration Rover (MER) and Mars Pathfinder (MPF) and the appropriate additions are made in the areas where physics are different from what the prior entry systems would encounter. These additions include the considerations for the high angle of attack of MSL EV, ablation of the heatshield during entry, turbulent boundary layer, and other aspects relevant to the flight performance of MSL. Details of the work, the supporting data and conclusions of the investigation are presented.

Nomenclature

α	Angle of attack, degrees
β	Angle of sideslip, degrees
β	$m/C_D A$, ballistic coefficient
γ	ratio of specific heats
C_A	Axial force coefficient, $F_{axial}/(Q_\infty S_{ref})$
C_L	Normal force coefficient, $F_{normal}/(Q_\infty S_{ref})$
C_m	Pitch moment coefficient, $M/(Q_\infty S_{ref} L_{ref})$
D	Capsule diameter, m
L_{ref}	Reference length, main diameter, m
M	Mach number, also used for moment of a force
p	pressure, Pa
Q	Dynamic pressure, $1/2\rho V^2$, Pa
RCS	Reaction Control System
Re	Reynolds number
ρ	Density, kg/m^3
S_{ref}	Reference area, frontal area, m^2
τ	shearing stress, Pa
Subscript	
∞	free-stream
D	based on diameter
w	wall

[*]Aerospace Engineer, Atmospheric Flight Entry Systems Branch, NASA Langley Research Center, AIAA Member.
[†]Aerospace Engineer, Atmospheric Flight Entry Systems Branch, NASA Langley Research Center, AIAA Member.
[‡]Senior Project Engineer, Analytical Mechanics Associates, Inc., Hampton, VA, 23666. AIAA Member.

American Institute of Aeronautics and Astronautics

I. Introduction

Mars Science Laboratory entry vehicle is different from its predecessors in a number of ways: its larger and heavier and it is designed to land much closer to its intended target. These considerations drove the design toward a lifting actively guided entry.[1] Lift is achieved by offsetting the vehicle's center of mass to a nominal location 0.3D aft of nose and 0.0215D off of the centerline. This results in a hypersonic trim at approximately 16 degrees and a hypersonic L/D of approximately 0.24. Bank angle and attitude rate control is enacted by a set of hydrazine thrusters on the rear of the vehicle. During flight the control system will execute a bank program to steer the vehicle to the landing site using aerodynamic lift. This is new at Mars,[2] as all prior vehicles were either nominally non-lifting systems (MER A-B, MPF, Mars Phoenix) or lifting un-guided systems (Viking 1 and 2).

As an aerodynamic system, MSL capsule presents several new questions that must be answered: are there any new physics, not of concern to prior missions, which might affect the trim angle of attack, lift and drag performance and control. This paper is focused on the investigation of static aerodynamics, leaving out the aspects related to control, such as pitch damping and aero-RCS interaction, which are discussed in other publications[3-][5] Because aerodynamics in hypersonic and supersonic regime are quantified largely by CFD tools, impact of modeling assumptions on the predicted trim characteristics was assessed. This sensitivity analysis and comparisons of predictions with data are discussed in the paper. The paper contains all static aerodynamic coefficients in use between onset of continuum and parachute opening.

II. Vehicle Description

The shape of MSL entry vehicle is derived from previous Mars missions. The heatshield is a 70-degree sphere-cone with bluntness radius 1/2 of the vehicle's base radius, and the backshell is a collection of truncated cones, appropriately sized to accommodate the payload. The outer surface contains features and components such as cruise and entry balance masses, which are not always flush, and is therefore more complex then simply a collection of spherical, conical and toroidal surfaces. Figure 1 shows assembled MSL aeroshell. For the purposes of this analysis the shape is simplified as shown in the figure 2. Effect of simplification on aerodynamics was assessed as shown further in the paper.

Figure 1. Assembled entry vehicle (held by space craft rotation fixture).

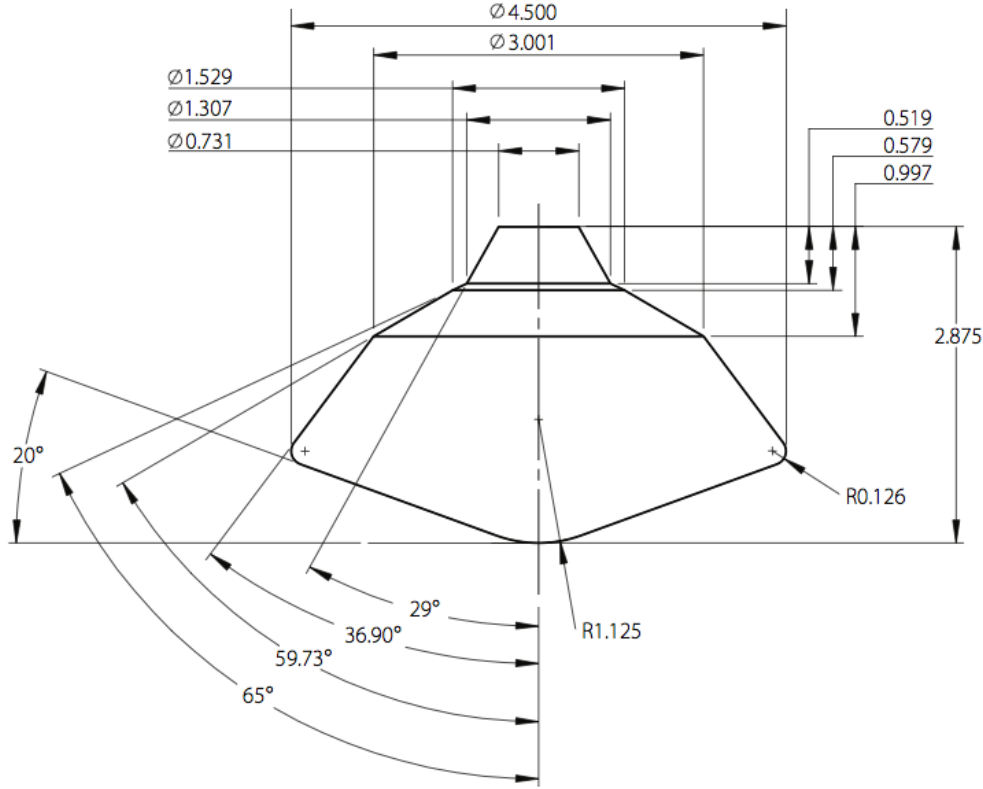American Institute of Aeronautics and Astronautics

Figure 2. (Simplified) entry vehicle OML dimensions (meters).

III.   Aerodynamic coefficients

Aerodynamic force is formulated in axial and normal components C_A and C_N as follows:

$$C_A = \frac{\int_{S_{front}} [(p - p_\infty)n_x + \tau_x]\, dS}{S_{ref}Q_\infty} \tag{1}$$

$$C_N = \frac{\int_{S_{front}} [(p - p_\infty)n_z + \tau_z]\, dS}{S_{ref}Q_\infty} \tag{2}$$

and the pitch moment coefficient is calculated as

$$C_{m,0} = \frac{\int_{S_{front}} [(p - p_\infty)(xn_z - zn_x) + z\tau_x - x\tau_z]\, dS}{S_{ref}L_{ref}Q_\infty} \tag{3}$$

Equations 1, 2, 3 are shown to emphasize three points. First - that the summation is done over the front of the capsule. This is done because CFD prediction of separated base flow is still uncertain and MSL aerodatabase uses an engineering base pressure model, described further. Secondly, calculations result in an integral of pressure coefficient, not absolute pressure. In the context of this work this makes the application of base pressure models more straight-forward. Thirdly - while it is true that supersonic and hypersonic aerodynamics of blunt shapes are dominated by pressure forces, the shear forces are not negligible. This is the case especially for the moment coefficient.

A.   Accounting for pressure on the base

Capsule flowfield includes a reacting, frequently non-equilibrium shock layer, expansions and re-compresions, lip shocks and hypersonic shear layers. Schematic of the flowfield is shown in the figure 3. None of the CFD

American Institute of Aeronautics and Astronautics

codes, available to the authors can handle all of these processes well. For example, LAURA[6] is shown to accurately capture attached forebody flow with the associated gas chemistry, but was not shown to predict base pressure well. Code OVERFLOW[10] is likely better at capturing base pressure, but for now at the expense of chemistry. Another code, which will be discussed further, FUN3D[12] is intended to help with many of these challenges, but was not ready in time for this work. Because of this, the effect of base pressure on MSL aerodynamics was accounted using the same method as in the earlier Mars Exploration Rover (MER) and Mars Pathfinder (MPF).[8]
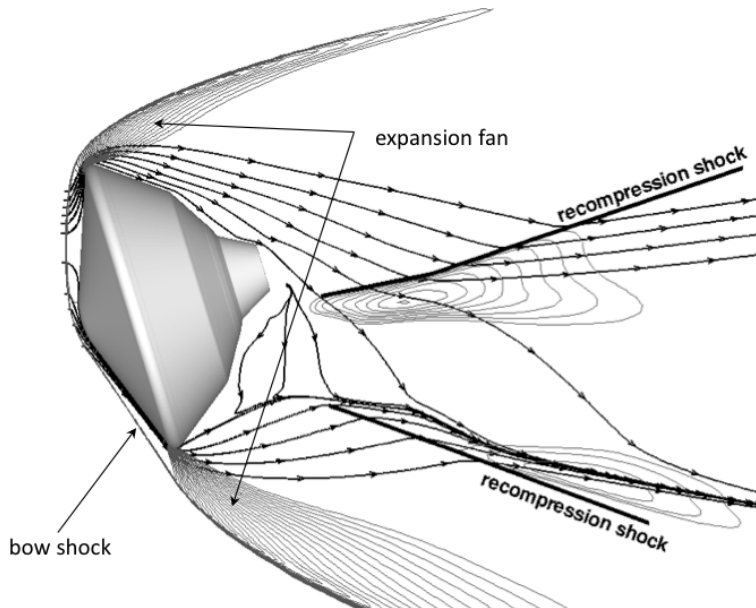

Figure 3. Features of flow around MSL in hypersonic regime

Base pressure correction is given as

$$-C_{A,base} = C_{p,b} = a_0 + \frac{a_1}{M_\infty} + \frac{a_2}{M_\infty^2} + \frac{a_3}{M_\infty^3} \tag{4}$$

where $a_0 = 8.325E{-}3$, $a_1 = 1.1293E{-}1$, $a_2 = -1.801$ and $a_3 = 1.2885$. this fit is derived from Viking lander flight data and was previously used for MPF and MER with good results. In terms of the sign convention, base pressure coefficient 4 is added to the axial force coefficient C_A such that at low Mach numbers the total axial coefficient is increased. At low speeds wake pressure is lower than free-stream, while at hypersonic speeds it can be higher than free-stream, as the fit suggests. No correction is added to the normal force or the pitching moment. It should be noted that the base correction does affect the pitching moment about vehicle's CG because of the off-axis CG of MSL.

IV. CFD Method and Sensitivities

Continuum supersonic and hypersonic regime static aerodynamic coefficients are obtained from Thin Layer Navier-Stokes simulations with Langley Aerothermal Upwind Relaxation Algorithm (LAURA). LAURA solutions use two-temperature non-equilibrium 8-specie Mars gas ($CO_2, CO, N_2, O_2, NO, C, N, O$) called in LAURA by *nplanet* flag of 1. At the wall the radiative equilibrium temperature boundary condition is used with wall emissivity $\varepsilon{=}0.89$ representative of a charred ablator. Supercatalytic wall boundary condition is enforced, requiring full recombination of free-stream CO_2 and N_2. Only the forebody aerodynamic coefficients are included in the database. Forebody solutions are obtained on a 7-block singularity-free grid. Blocks are dimensioned such that the 20x20 nose cap is surrounded by three blocks of dimensions 20x20, followed by a tier of blocks, whose dimensions are 28x20. All blocks have 64 cells in the wall-normal direction. LAURA code has a built in method to adopt the computational mesh to the shock layer and to the boundary layer. The default adoption criteria were used and they result in a grid, such that 80% cells are inside the shocklayer, and the wall spacing Reynolds number is on the order of unity (see, for example,

American Institute of Aeronautics and Astronautics

figure 26). This generally results in dense packing of points at the wall, suitable for aeroheating calculations and perhaps excessive for aerodynamics, however this does not cause a concern for aerodynamics. In the course of the solution point-implicit and line-implicit relaxation algorithms are used. Default eigenvalue limiters and relaxation factors are used throughout. When a grid adaption and a consecutive convergence of the solution returns the same pitching moment coefficient as before to three decimal places, the solution is considered to be converged. Exception to this rule is any case at zero angle of attack: because moments are trivial, the axial force coefficient is used instead.

A. Continuum Data Map

The collection of static aerodynamic coefficients, computed with LAURA was entered into the MSL aerodynamics database for use by POST.[9] The aerodatabase contains supersonic and hypersonic data at discrete pairs of total angle of attack and Mach number, shown in the figure 4. Data is intentionally clustered around the design trim point. Since the data proved to be well-behaved with angle of attack - the clustering is perhaps a little excessive, and can be thought of as a good internal consistency check. All data labeled MSL_- is calculated for MSL on 05-22 nominal trajectory. All data labeled $MER\_v.9.1$ is a carryover from MER aerodatabase. Only the data at low angles of attack (11 degrees and below) was carried over and it is outside of the nominal flight regime of MSL entry capsule, yet sufficiently applicable for its intended use. Flight regime is specified by either velocity or Mach number, as appropriate (check regimes).
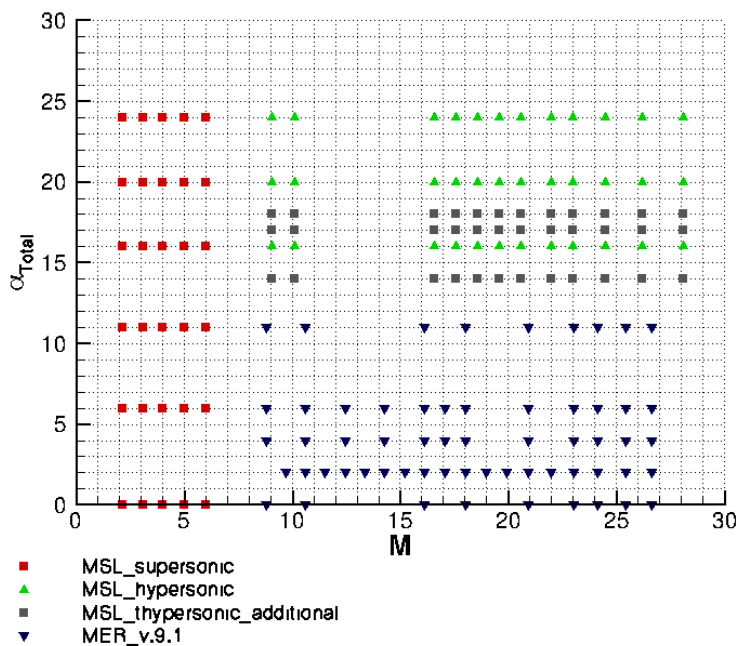

Figure 4. Map of LAURA data in supersonic and hypersonic regime.

B. Use of TLNS

Solutions in the aerodatabase are of a so-called Thin Layer Navier-Stokes type. This means that the viscous terms, containing derivatives in surface-tangent directions were omitted from the discretized equations. At the time when this work was done, this practice was common for aeroheating and aerodynamic calculations for blunt cones. To verify that the numerical predictions of aerodynamics for MSL do not dependent on this detail, calculations were carried out at Mach 4 condition with all viscous terms and with only the viscous terms containing surface-normal derivatives. As the figures 5 and 6 indicate, no significant change

American Institute of Aeronautics and Astronautics

in predicted axial force or trim is associated with inclusion of those terms. Static aerodynamic coefficients in these figures include contribution due to base pressure.
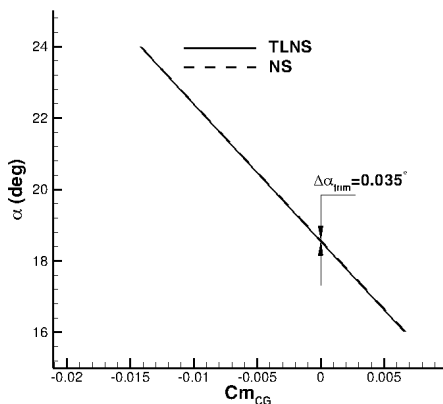

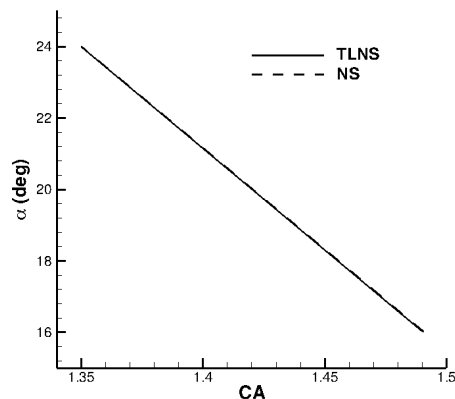**Figure 5. Effect of viscous terms on trim**

Figure 6. Effect of viscous terms on axial force

Table 1. Supersonic (Mach=4) 05-22 conditions for TLNS vs. N-S comparison

α, deg	$V_\infty, m/s$	$\rho_\infty, kg/m^3$	T_∞, K
16	892	.003803	189.9
24	892	.003803	189.9

C. Effect of real gas at supersonic conditions

While the database carries only the real gas solutions irrespective of the regime, perfect gas model with an effective γ[13] was used for comparison at supersonic Mach 4 condition. This approach uses perfect gas model with the ratio of specific heats evaluated using equilibrium chemistry at temperature and pressure behind the normal shock. Results of these calculations, as well as the resultant shock shape change are summarized in figures 7 and 8. Overall there is little sensitivity to gas model at supersonic speeds for a reasonable choice of effective γ.

D. Non-equilibrium Processes

The range of shock velocity and stagnation pressure during Mars atmosphere entry present a diverse thermochemical environment. At higher velocities, before maximum deceleration, most of atmospheric CO_2 is dissociated by the shock, and the shocklayer pressure is sufficiently low, allowing some degree of thermal non-equilibrium in the flow. As the shocklayer pressure builds to its peak of around 1/3 atmosphere the flow is mostly thermally equilibrium, and CO_2 is still fully dissociated. Further deceleration reduces shock strength, gradually increasing the amount of CO_2 in the shocklayer, and the stagnation pressure drops, creating conditions for thermally non-equilibrium flow. Because of this, static aerodynamic coefficients are obtained with CFD solutions, which allowed thermochemical non-equilibrium. While generating initial solutions for MSL two two-temperature relaxation models were used for CO_2(unintentionally), Millican-White[14] and Camac.[15] It was found that the choice of models affects static aerodynamics significantly between Mach 15 and 5, with a peak at velocity of 2000 m/sec (around Mach 9). There is ample undissociated CO_2 in the shocklayer at these conditions, and modeling of thermal relaxation for this molecule becomes important. The two models predict different relaxation rate, resulting in different shock stand-off distance. Figure 10 shows the difference in shock stand-off at the same free-stream condition between the two models. Shock stand-off is a significant factor in establishing surface pressure distribution, and therefore, static aerodynamics. Camac model is believed to be correct and was used in the past for Mars missions, while Millican-White model is
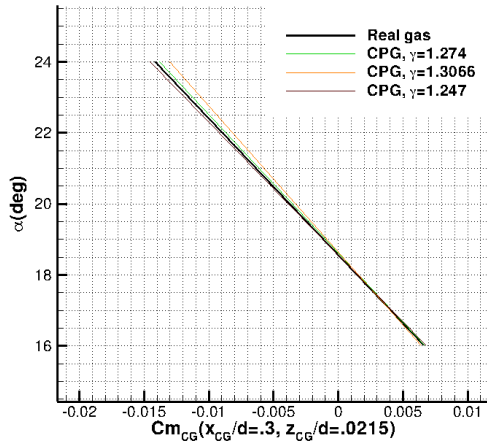
American Institute of Aeronautics and Astronautics

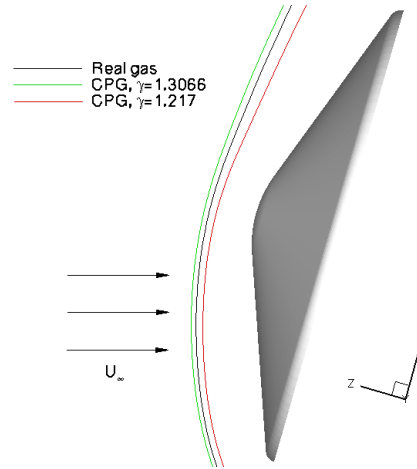**Figure 7. Effect of gas models on supersonic trim**

Figure 8. Effect of gas models on shock shape

suitable for diatomic molecules and is not valid for CO_2. Figure 9 shows the static stability curves, revealing a sensitivity of trim, slacker stability at higher angles for Millican-White model. Figure 10 shows the vehicle at zero angle of attack, but the disparate shock location is, off course, maintained throughout the range of α. While there's little doubt, that the Camac model is more accurate for Mars entry simulations, there's little data to definitively estimate the accuracy of predicted relaxation rates. Because of this, the aerodynamic uncertainties applied to MSL hypersonic static coefficients are adjusted to bound this sensitivity.
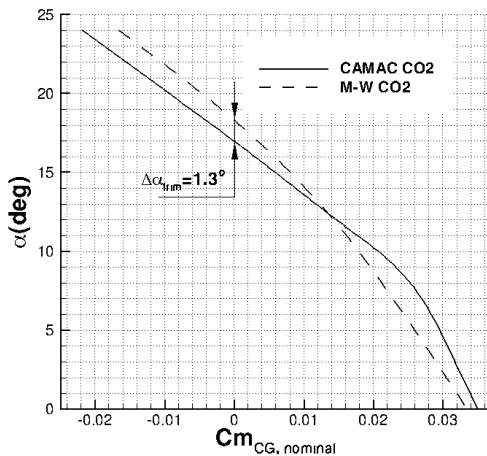

Figure 9. Effect of gas models on supersonic trim
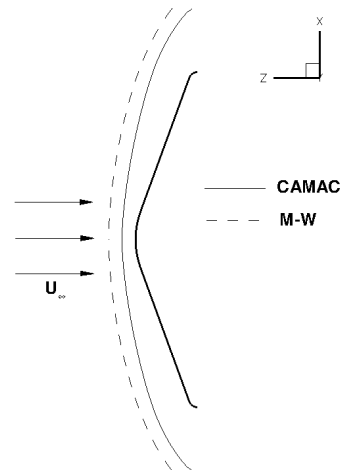

Figure 10. Effect of gas models on shock shape

E. Effect of turbulence

MSL is expected to develop a turbulent boundary layer early in its entry and should maintain it for most of the pressure pulse. Figure 11 shows the variation of smooth wall transition parameter Re_θ in the capsule's pitch plane along the early part of 08-02 design trajectory. The last solution shown at 80 seconds is just short of the maximum dynamic pressure, and Re_θ is still climbing at that point. MSL is designed for a fully turbulent heat pulse because of a prolonged flight in a region where Re_θ exceeds any commonly accepted for onset of turbulence on blunt shapes.[16]

American Institute of Aeronautics and Astronautics

Turbulence can affect static aerodynamics through two mechanisms, namely the thickening of the boundary layer, which results in a greater apparent cone angle, and an increase in wall shear, which will result in an additional moment about the moment reference point. Both of these effects are greatest on the leeside of the heatshield, and should result in a moment, that will tend to increase the vehicle's angle of attack (see figure 12). In order to determine possible effect of a thicker boundary layer and higher shearing stress due to turbulence, several solutions were evaluated using Baldwin-Lomax turbulence model. Baldwin-Lomax turbulence model is shown in multiple experiments[17−22] to accurately predict heating on blunt shapes, but there is no sufficient data to conclude that this model captures shear stress and displacement of the boundary layer accurately. Testing MSL shape on a force-moment balance in AEDC Wind Tunnel No. 9 similarly to the campaign, described in[17] would provide relevant data.

Effect of turbulence on trim angle of attack for several free-stream velocities is shown in the figure 12. Calculations indicate an increase of the trim angle of attack by $\Delta\alpha_{trim} \approx 1$ degree in some cases. This change is consistent with what was expected of mechanisms, also described in the figure 12. Analysis of solutions showed that the predicted effects of boundary layer displacement and of increased shear are close in magnitude. Effects of turbulence on the axial force are not shown, but calculations indicate axial force coefficient to be affected in the fourth decimal place.
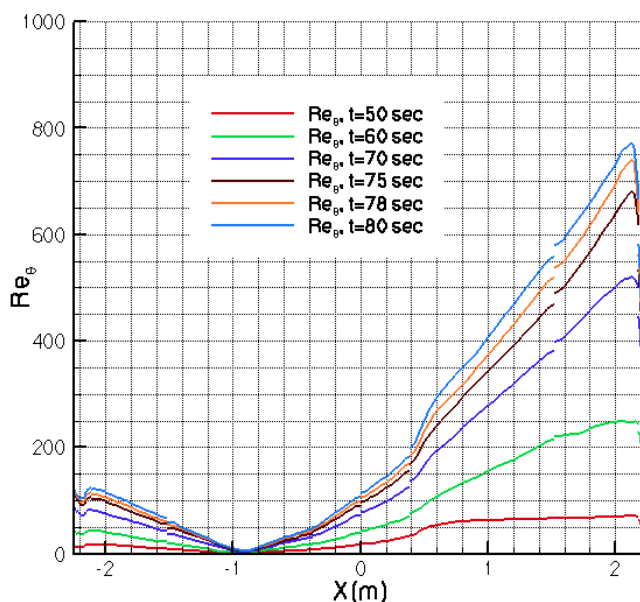

Figure 11. Smooth wall transition parameter

V.   Sensitivity to Shape

A.   Design Changes

Over the period in which this work developed, the aeroshell has evolved significantly. Main changes are concentrated on the aftbody, as it's grown to accommodate a larger landing system. Figures 13 and 14 compare the aeroshell shape, which was used for the aerodatabase to the current baseline, termed OML 13F. Most notable are the increased height of the backshell and the addition of the Parachute Closeout Cone (PCC). The forebody remained nearly unchanged, except for some detail near the shoulder. Changes to the shoulder are dictated by the need to accommodate transition of Thermal Protection System (TPS) material and substructure from the forebody cone onto the shoulder and onto the first aftbody cone. This re-profiling of the shoulder resulted in it no longer being constant in radius. Result of these changes is a 3.5 mm increase in the base diameter of the capsule. Magnitude of this increase, as well as the changes in the profile of the shoulder itself are not significant. As previously mentioned, the shoulder will change shape during flight. Expected recession may be as high as 2 cm and may be uneven.

Changes in the shape of the aftbody do not affect the aerodatabase because the CFD aftbody solution is
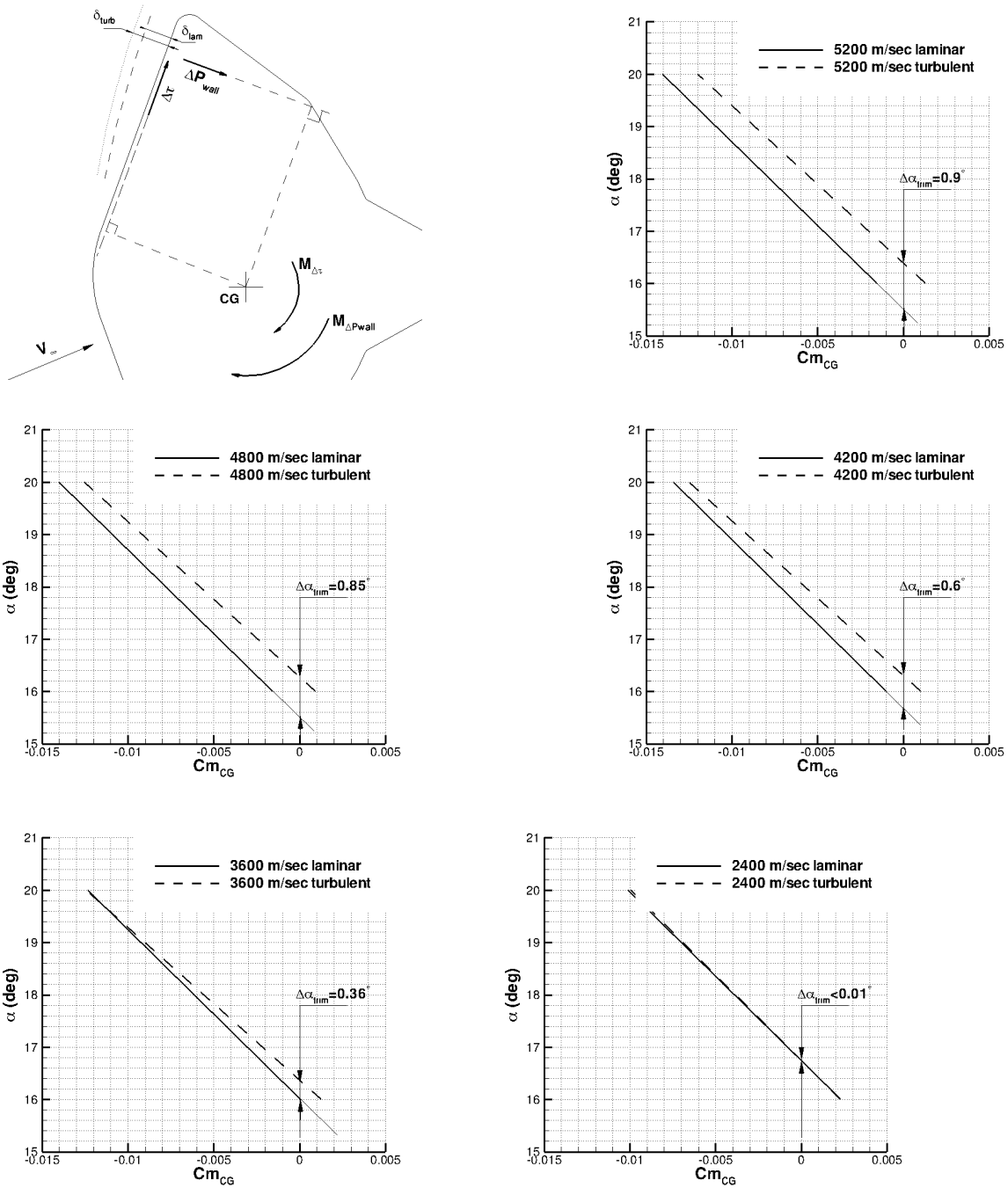
American Institute of Aeronautics and Astronautics

Figure 12. Effect of turbulence on capsule moment

not being used, and base pressure correction is used instead. Comparisons of calculations with the aftbody contribution and with the aftbody contribution replaced with the base correction are shown in figures 15 and 16. These figures show results for LAURA and OVERFLOW codes. While Mach 3 results show greater variance, the bulk of it is due to lack of shock adaptation in the shown OVERFLOW solutions. Overall, the results indicate that it is acceptable to apply the supersonic base correction to the CA.
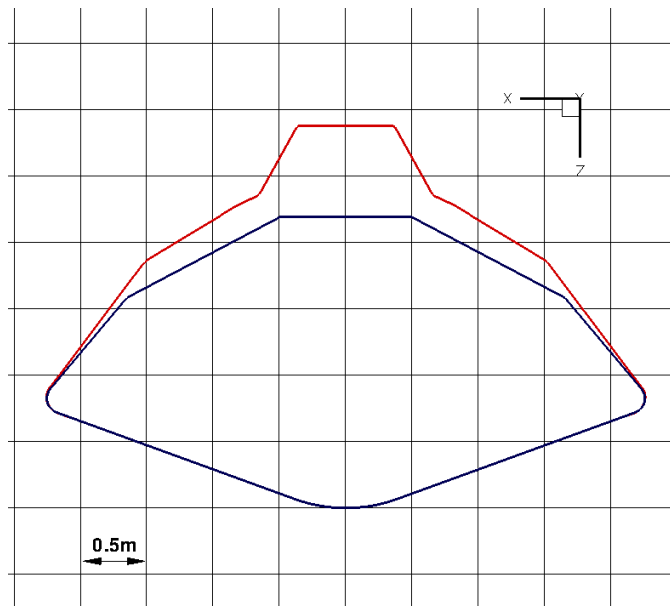
Figure 13. Comparison of capsule OML used for the database (blue) and current OML 13F (red)
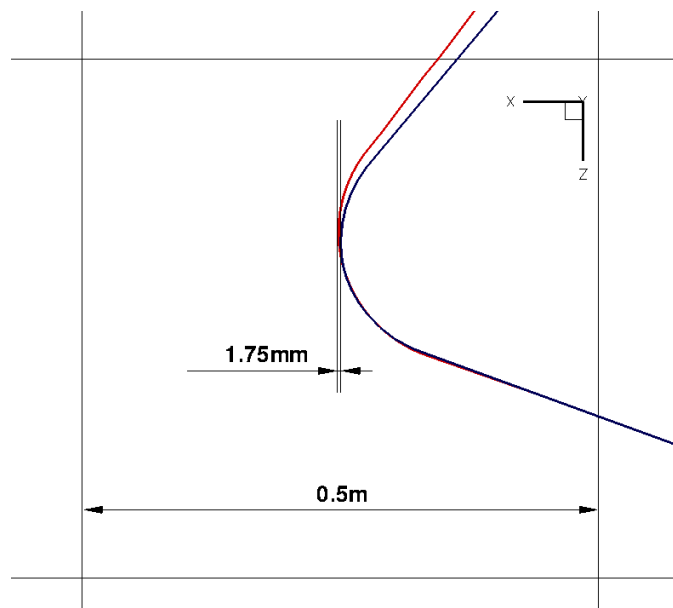

Figure 14. Comparison near shoulder of OML used for the database (blue) and current OML 13F (red)

B. Effect of heatshield ablation

During atmospheric entry the forebody TPS will loose a part of its thickness. The conservative estimate of TPS recession was carried out for for sizing purposes, and it suggested up to a 0.8 inch recession on the forebody leeside, in the area of high turbulent heating. TPS recession is not expected to be uniform over the forebody because of non-uniform heating. To determine the possible effect of this shape change on static aerodynamics, the recession map is applied to the nominal OML and calculations are carried out for hypersonic regime. Forebody ablation can affect aerodynamic stability mainly through two mechanisms. Because the material is lost over a large section of the heatshield, the center of mass of the capsule will shift. Secondly, the change in the shape itself in relation to the nominal center of mass will result in some change in the moment of surface forces. The magnitude of changes in trim angle due to both of these mechanisms
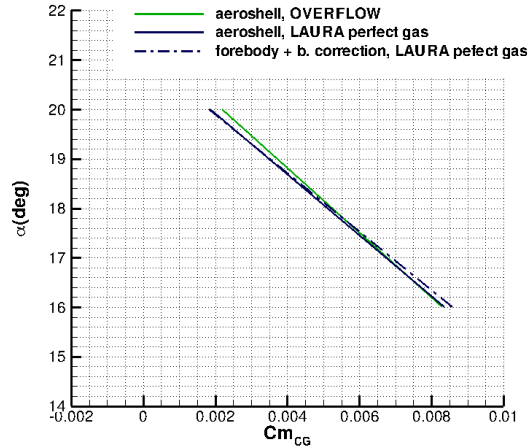
American Institute of Aeronautics and Astronautics

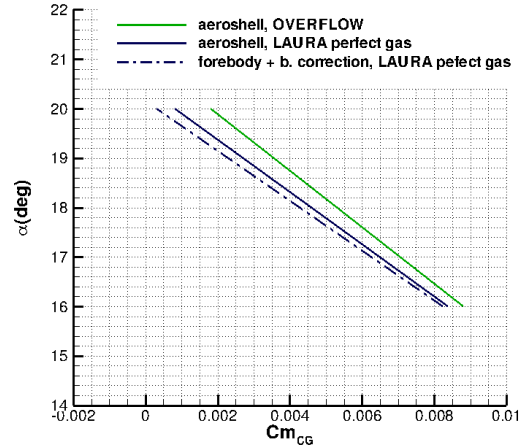**Figure 15. Mach 2 capsule moment, various methods**

Figure 16. Mach 3 capsule moment, various methods

needed to be quantified. The TPS recession estimate, used here did not have sufficient spatial resolution since the recession was calculated only for the windside and leeside rays at the time the work was done. Linear interpolation in the angular sense was used to fill the missing area, under the assumption that the heat flux and recession will vary in some like manner. The resultant slab of lost TPS material has an estimated mass of 56.6 kg (for nominal PICA density of 0.265 g/cc), with the center of mass of $z_{cg} = $ -.504m, $x_{cg} = $ .199m. Capsule's nominal CG is located at $z_{cg} = $ -1.35m, $x_{cg} = $ -.09675m and its initial mass is estimated at 3380 kg. The new CG location is at $z_{cg} = $ -1.364m, $x_{cg} = $ -.1018m. Just from this shift of CG the change of the hypersonic trim point from is from 16.34 degrees to 16.91 degrees. In addition, hypersonic LAURA calculations were carried out to determine the shift in the trim curve. The shift due to change of shape is fro 16.34 degrees to 16.32 degrees, or a barely noticeable reduction. This is consistent with earlier Newtonian analysis, which shows a similar trend: the loss of material on the lee side of the heatshield results in reduced angle of attack. Effects of shape change and mass loss are opposing, with the latter being more pronounced.

C.   Effect of capsule deformation under aerodynamic load

MSL entry system is designed for trajectories with up to 15 Earth G's deceleration load. Peak load will occur near Mach 18 in hypersonic regime. Because the capsule has offset CG to generate lift, neither deformation nor its effect on aerodynamic characteristics has to be symmetric. To estimate the possible magnitude of change, the finite element analysis of MSL aeroshell under 12.2 G's loading on the then-current 06-05 nominal entry trajectory was carried out at LMA. Figures 17 and 18 show (exaggerated) the results of this analysis. The deformed profile was applied to the CFD grid to determine changes in trim. The plot of the pitch stability in the figure 18 takes into account the movement of the deforming aeroshell with respect to the payload. The assumption here is that massless aeroshell moves relative to the nominal CG, where all entry mass is concentrated, and that point is fixed relative to the Backshell Interface Plate (BIP) at the rear of the capsule. In reality the heatshield and backshell move under load in relation to the internals, such as the rover, the descend stage, fuel tanks etc. The moving mass is roughly a metric ton, or a third of the entry system mass. The plot of the static stability curves shows the change in the trim point by roughly 1/2 a degree.

VI.   Grid Sensitivity

Changes in the aeorshell geometry led to re-making of the structured CFD grid used in most calculations. Much of the work on aerodynamics was done using the older grid, and sensitivity to the grid change needed to be established.
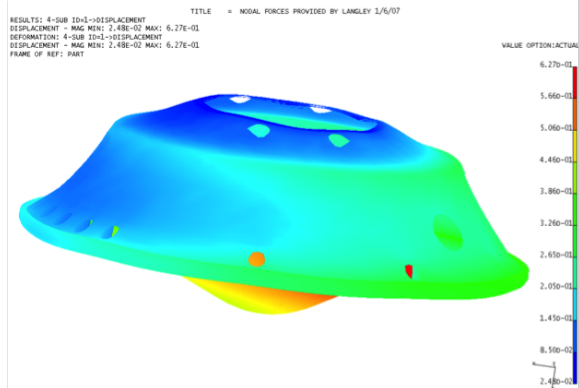
American Institute of Aeronautics and Astronautics

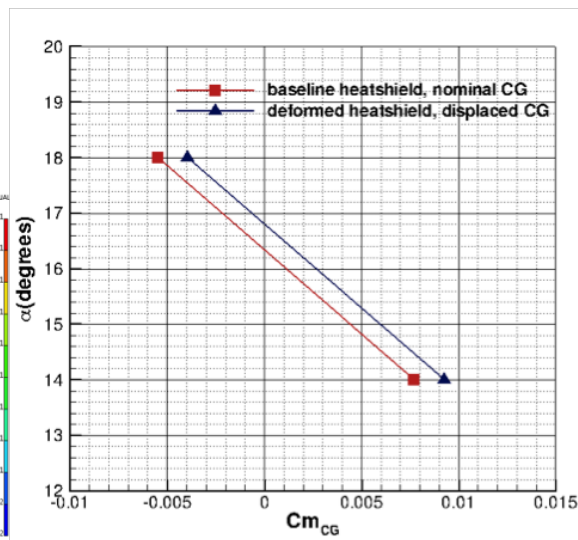**Figure 17. Capsule deformation (exaggerated) showing asymmetry**

Figure 18. Effect of deformation on stability

A. Grid topology, grid refinement

Forebody solutions for the aerodynamic database are obtained on a 7-block singularity-free grid. Blocks are dimensioned such that the 20x20 nose cap is surrounded by three blocks of dimensions 20x20, followed by a tier of blocks, whose dimensions are 28x20. All blocks have 64 cells in the wall-normal direction. Grid layout is shown in figure 23. Figure 24 shows the layout of MER grid, which was used in development of the MER database and was sufficient for low angles of attack. Layout of the current OML13F forebody grid is shown in the figure 25. This newer grid is different in resolution, as well as reflects some of the shape differences, discussed earlier. Comparisons of predicted trim characteristics at Mach 4, computed with the grids in the figures 23 and 25 are shown in figures 19 and 20. The figure 19 indicates the comparison of the trim curve between the grid, currently used in the aerodatabase with that, computed on OML13F grid. The OML13F used in this calculation was coarsened to match the grid used in the aerodatabase (see above). To determine the effect of grid refinement this coarsened OML13F grid was compared to a finer version, results are shown in the figure 20. These comparisons suggest that the gridding requirements for a 70-degree sphere-cone at high angle of attack, such as MSL, can be significantly different than the requirements for the same body at a lower angle of attack.

B. Effect of excluding the wake part of the grid

LAURA solutions for the aerodatabase were computed on a forebody mesh, which covers the volume ahead of the capsule's maximum diameter. At a high angle of attack and low Mach number the sonic line may cross the base plane, which was used to define the exit of the CFD domain, resulting in subsonic outflow from the CFD domain. At the exit, LAURA uses a simplified outflow boundary condition, suitable for supersonic outflow but not for subsonic outflow. To determine whether this has any measurable effect on the predicted static aerodynamics, comparisons were done at Mach 2 for angles of attack 16, 20 and 24 degrees and at Mach 4 at angles of attack 16 and 24 degrees with and without the wake part of the grid in the simulation. Figures 22 and 22 show the difference between the two types of simulations at Mach 4 and Mach 2. The pitching moment coefficient uses forebody CFD data, but in the case of the "aftshell included" simulation the forebody simulation was coupled with a wake flow simulation, thus avoiding the ill-posedness of the outflow boundary. The difference of less then .05 degree at these two Mach numbers illustrates that if the sonic line intersects the exit of the computational domain no significant error in predicted trim characteristics of the forebody will result.
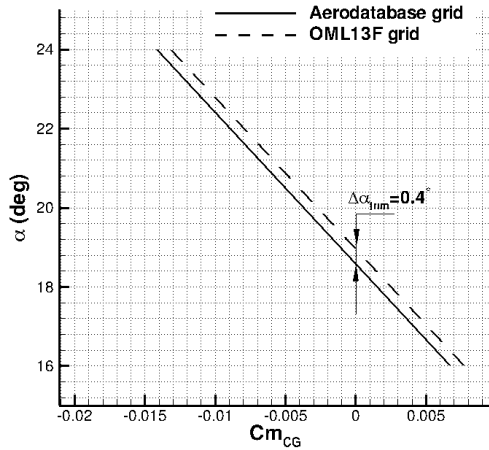
American Institute of Aeronautics and Astronautics

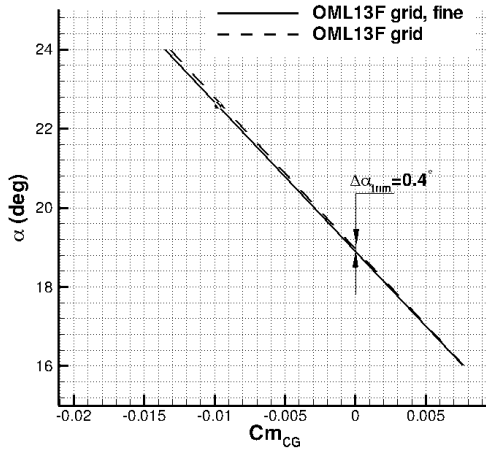**Figure 19. Effect of grid topology on trim**

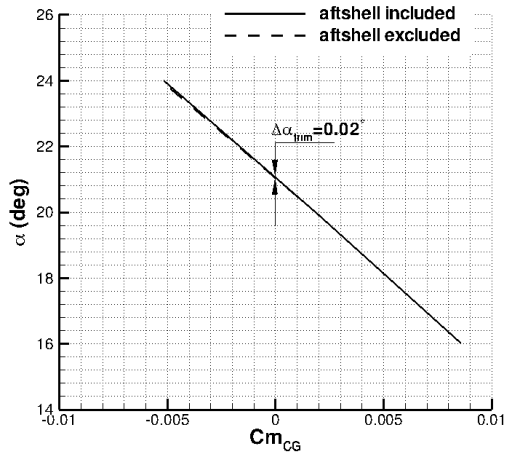**Figure 20. Effect of grid refinement on trim**

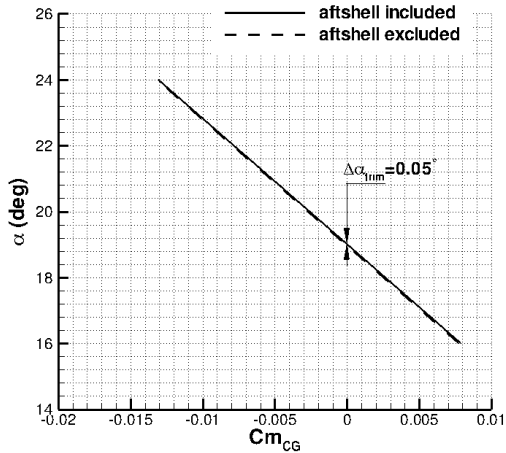**Figure 21. Effect of wake exclusion at Mach 2**

Figure 22. Effect of wake exclusion at Mach 4

VII. Trajectory Sensitivity

Since the 05-22 trajectory was current, the capsule entry mass has gone up by 20% (2804 to 3380 kg). Figures 27, 28, 29, and 30 illustrate changes this caused in the trajectory space going from the 05-22 to the more recent 08-TPS-02.

Because it was not possible to adapt aerodatabase in real time to stay current with the changes in the design trajectory, 05-22 was kept as the aerodatabase trajectory, but spot checks are done to determine if any significant issues arise. As evidenced by the figures 27, 28, 29, and 30, the differences in density are most pronounced between 05-22 and 07-25 at hypersonic speed, and between 05-22 and 06-05 at supersonic speed. Two conditions were selected for the test cases: hypersonic condition at a free-stream velocity V_∞=3600 m/s (05-22 and 07-25) and a supersonic condition at M=4 (05-22 and 06-05). Tables 2 and 3 show the conditions.

Figure 31 illustrates static stability at Mach 4 for the two trajectories. It indicates very little if any variance due to the change of condition. Figure 32 confirms the same story for a hypersonic flight condition.
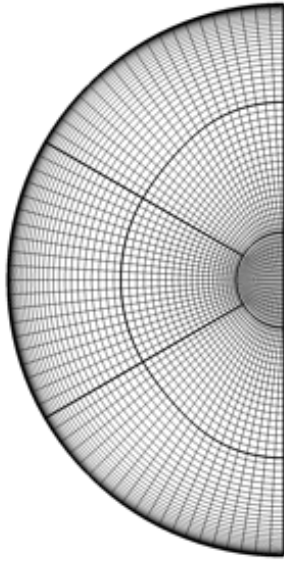
American Institute of Aeronautics and Astronautics
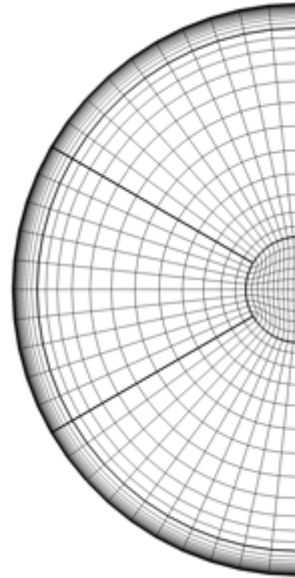
Figure 23. MSL grid layout

Figure 24. MER grid layout

Table 2. Supersonic Mach 4 condition for 05-22 and 06-05 nominal

Trajectory	$V_\infty, m/s$	$\rho_\infty, kg/m^3$	T_∞, K
05-22 nominal	875.3	.00380	189.8
06-05 nominal	894.7	.00300	198.1

VIII. Comparison of the CFD and Experimental Data

Comparison of CFD predictions with experimental data was carried out to gauge accuracy of lift, drag and trim characteristics. Comparisons are shown in axial and normal force coefficients, as a measure of lift and drag characteristics, and the pitching moment about MSL's nominal center of gravity as a measure of expected trim point. Comparisons are shown for M = 2.5 and M = 10 conditions. Data is collected in air, perfect gas. Figure 33 shows a comparisons of LAURA (air and CO2) for MSL and Viking shapes and Viking Mach 10 wind tunnel data. There's a good agreement between CFD and data, and there's an indication of greater static stability in CO2 atmosphere. This is expected and is a result of a lower ratio of specific heats, and subsequently smaller shock stand-off as compared to air as perfect gas. Comparison of predicted aerodynamics with flight data is discussed by Gnoffo et.al.[23] Agreement of aerodynamic predictions and observed behavior at high enthalpy entry conditions was demonstrated, lending credence to aerodynamics in that regime. In addition, work by Schoenenberger[?] showed that the current set of MSL aerodynamic predictions agrees well with Viking flight data.
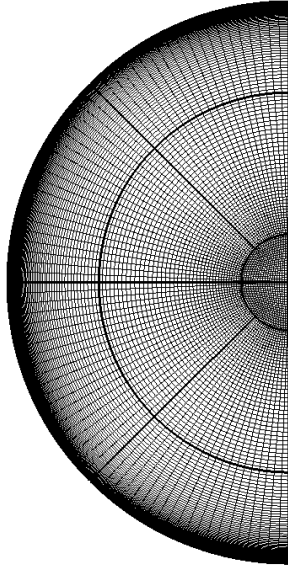
American Institute of Aeronautics and Astronautics
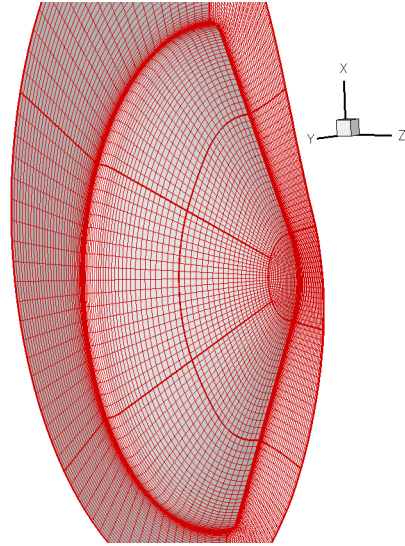
Figure 25. OML13F grid layout

Figure 26. Example of adapted grid

Table 3. Hypersonic (Mach≈16.5) conditions for 05-22 and 07-25v2 nominal

Trajectory	$V_\infty, m/s$	$\rho_\infty, kg/m^3$	T_∞, K
05-22 nominal	3600	.001934	186.8
07-25 nominal	3600	.002611	180.0

IX. Hypersonic and Supersonic Data

Tables 4, 5 and 6 list the MSL values that are currently in the aerodatabase. Free-stream conditions as used are also tabulated. Note, that the Mach number in the tables is a LAURA real gas Mach number which is different from the perfect gas Mach number reported by POST. POST Mach number is used in the place of LAURA Mach number in the database to be consistent with the simulation. Pitching moment coefficient uses the Moment Reference Point (MRP) consistent with Mars Pathfinder (MPF), for which X/D=.2498, (1.124 m aft of nose for a 4.5 m diameter aeroshell). MRP has no radial offset. In the aerodatabase all hypersonic data is given relative to this Pathfinder MRP, however, all supersonic data is referenced to the nose, and shifted to the MPF MRP by a separate step. Data in tables 4, 5 and 6 is for forebody only; contribution of aftbody to static aerodynamics at supersonic speeds is handled through base pressure correction. In addition to the data, shown in the figure 4, the aerodatabase contains Viking wind tunnel data (TR-3709014) covering α=0, 6, 11, 16, 20 and 24 degrees at Mach 1.5 through 0.4.

American Institute of Aeronautics and Astronautics
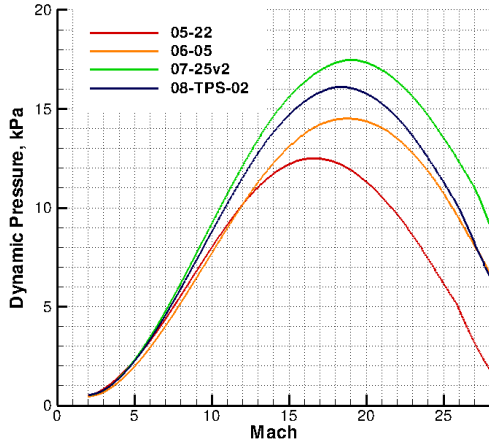
Figure 27. MSL trajectory Mach-Q space
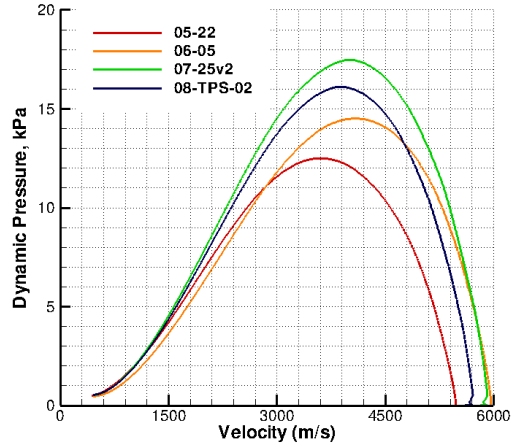
Figure 28. MSL trajectory V-Q space
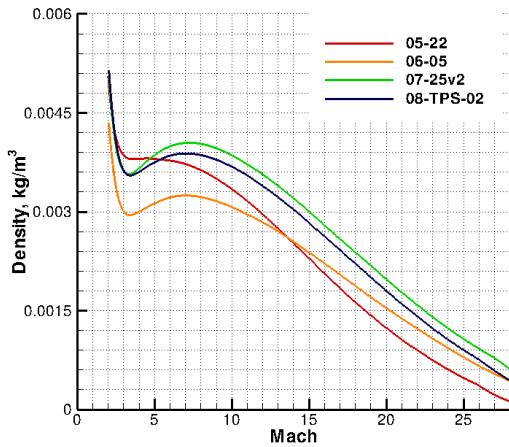
Figure 29. MSL trajectory Mach-ρ space
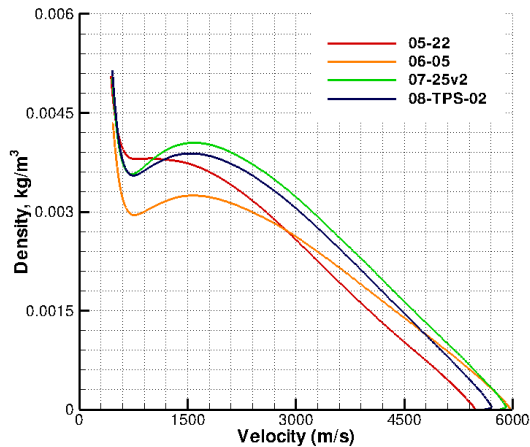
Figure 30. MSL trajectory V-ρ space

X.   Conclusions

Analysis of static aerodynamics from the onset of continuum flow through parachute opening is presented. The method was largely derived from prior Mars missions Mars Pathfinder and Mars Exploration Rover. Analysis of sensitivity to modeling assumptions and physics that are particular to MSL entry were carried out. Static aerodynamics were found to behave well at high angles of attack, particular to MSL flight scenario. Effects of heatshield ablation and deformation of the aeroshell were assessed, and found to be fairly minor. An unexpected sensitivity to physical modeling of CO2 molecule was found in the regime of low hypersonic flight, where abundant CO2 and sufficiently low pressure make thermal relaxation a strong driver of shock standoff and pressures. It was found that the turbulent boundary layer may have an appreciable effect on MSL trim, though we lack data to confirm CFD predictions in this case. Comparisons of CFD predictions with data shows good agreement both for the case of perfect gas and for high-enthalpy reacting environment. Aerodynamic uncertainties, applied to the model sufficiently cover the observed differences and sensitivities.

American Institute of Aeronautics and Astronautics
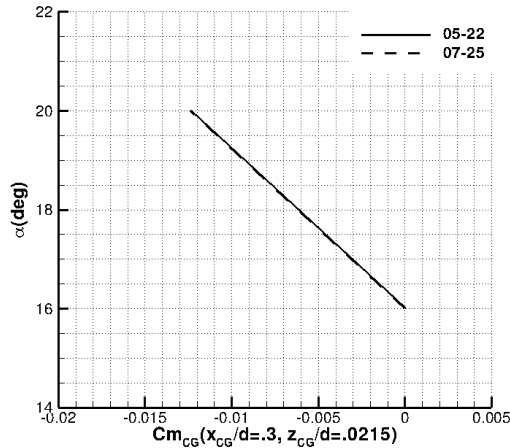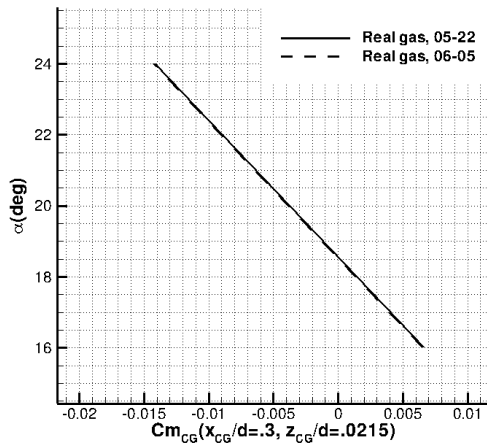
Figure 31. Static stability at Mach 4 for 05-22, 06-05 trajectories

Figure 32. Static stability at Mach 16 for 05-22, 07-25 trajectories
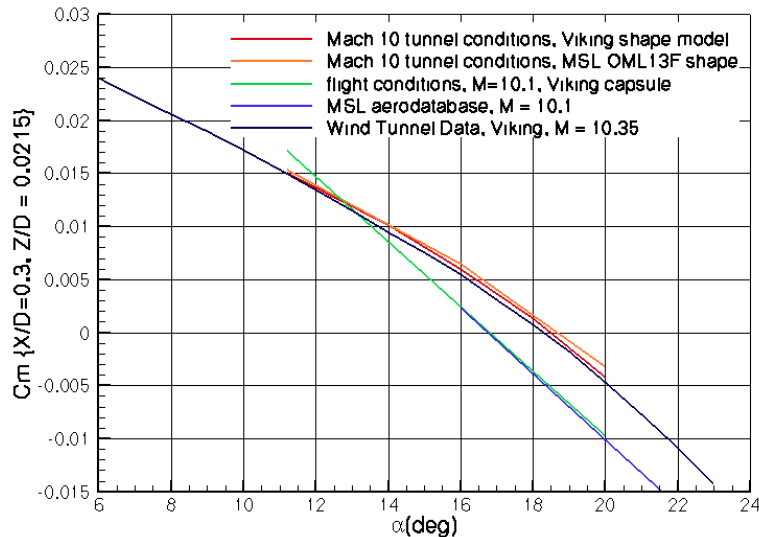
Figure 33. Pitching moment near M=10 for various datasets (MSL MRP).

References

[1]Steltzner, A., et al, Mars Science Laboratory Entry, Descent and Landing System, IEEE Paper 2006-1307, IEEE Aerospace Conference, Big Sky, Montana, March 2006.

[2]Mary Kae Lockwood, Ken Sutton, Ram Prabhu, Richard W. Powell, Claude A. Graves, Chirold Epp, Gilbert L. Carman, Entry Configurations and Performance Comparisons for the Mars Smart Lander, AIAA Atmospheric Flight Mechanics Conference and Exhibit, AIAA 2002-4407 5-8 August 2002, Monterey, California

[3]Schoenenberger, M., Yates, L., Hathaway, W., Dynamic Stability Testing of the Mars Science Laboratory Entry Capsule, AIAA 2009-3917, 2009

[4]Schoenenberger, M., Dyakonov, A., Buning, P., Scallion, W., and Van Norman, J., Aero- dynamic Challenges for the Mars Science Laboratory Entry, Descent and Landing, AIAA 2009-3914, 2009.

[5]Dyakonov, A. A., Schoenenberger, M., Scallion, W. I., Van Norman, J., Novak, L., and Tang, C., Aerodynamic Interference Due to MSL Reaction Control System, AIAA 2009-3915, 2009.

[6]Cheatwood, F. M. and Gnoffo, P. A., Users Manual for the Langley Aerothermodynamic Upwind Relaxation Algorithm (LAURA), NASA TM 4674, 1996.

[7]Riley, C. and Cheatwood, F., Distributed-Memory Computing with the Langley Aerothermo- dynamic Upwind Relaxation Algorithm (LAURA), Advances in Engineering Software, Vol. 29, No. 3-6, July 1998, pp. 317324.

American Institute of Aeronautics and Astronautics

[8]Mitcheltree, R. M., Corrections to Drag Coefficient Due to Base Pressure, Internal memo, scan of hardcopy: Corrections to drag coefficient due to base pressure.pdf, NASA LaRC, Mars Pathfinder Mission, 1995.

[9]Brauer, G. L., Cornick, D. E., and Stevenson, R., Capabilities and Applications of the Program to Optimize Simulated Trajectories (POST), NASA CR 2770, February 1977

[10]Nichols, R. H. and Buning, P. G., Users Manual for OVERFLOW 2.1 .

[11]Nichols, R. H. and Buning, P. G., Solver and Turbulence Model Upgrades to OVERFLOW2 for Unsteady and High-Speed Applications, AIAA 2006-2824, 2006.

[12]FUN3D User's Manual, http://fun3d.larc.nasa.gov/

[13]Sutton, K., $SV\_Mars9703.f$

[14]Millican, R.C. and White, D.R., Systematics of Vibrational Relaxation, Journal of Chemical Physics, Vol. 39, No. 12, p. 3209.

[15]Camac, M. and ed. Hall J.G., CO2 Relaxation Process in Shock Waves, Fundamental Phenomena in Hypersonic Flow, Cornell Univ. Press, Ithaca, New York, 1966.

[16]Hollis, B.R., Blunt-Body Entry Vehicle Aerothermodynamics, Journal of Spacecraft and Rockets, 2012, Vol. 49 no.3, p Vol. 39, No. 12, p. 435.

[17]Hollis, B. R. and Collier, A. S., Turbulent Aeroheating Testing of Mars Science Laboratory Entry Vehicle in Perfect-Gas Nitrogen, AIAA Paper 2007-1208, AIAA Aerospace Sciences Meeting and Exhibit, Reno, Nevada, January 2007

[18]Liechty, D. S. and Hollis, Mars Science Laboratory Experimental Aerothermodynamics with Effects of Cavities and Control Surfaces, Journal of Spacecraft and Rockets, Vol. 43, No. 2, March-April, 2006, pp. 340-353

[19]Hollis, B. R., Liechty, D. S., Wright, M. J., Holden, M. S., Wadhams, T. P., MacLean, M., and Dyakonov, A.A., Transition Onset and Turbulent Heating Measurements for the Mars Science Laboratory Entry Vehicle, AIAA Paper 2005-1437, AIAA Aerospace Sciences Meeting and Exhibit, Reno, Nevada, January 2005.

[20]Liechty, D. S. and Hollis, B. R., Heat Shield Cavity Parametric Experimental Aeroheating for a Proposed Mars Smart Lander Aeroshell, AIAA Paper 2002-2746, AIAA Fluid Dynamics Conference and Exhibit, St. Louis, Missouri, June 2002.

[21]Hollis, B. R. and Liechty, D. S., Boundary Layer Transition Correlations and Aeroheating Predictions for Mars Smart Lander, AIAA Paper 2002-2745, AIAA Fluid Dynamics Conference and Exhibit, St. Louis, Missouri, June 2002.

[22]Wright, M. J., Olejniczak, J., Brown, J. L., Hornung, H. G., and Edquist, K. T., Computational Modeling of T5 Laminar and Turbulent Heating Data on Blunt Cones, Part 2: Mars Applications, AIAA Paper 2005-0177, AIAA Aerospace Sciences Meeting and Exhibit, Reno, Nevada, January 2005.

[23]Gnoffo, P. A., Braun, R. D., Weilmuenster, J. K., Mitcheltree, R. A., Engelund, W. C., and Powell, R. W., Prediction and Validation of Mars Pathfinder Hypersonic Aerodynamic Database, Journal of Spacecraft and Rockets, Vol. 36, No. 3, May-June 1999, pp. 367373.

Table 4. Supersonic forebody LAURA data, MRP X/D = 0.0, Z/D = 0.0

α_{total}	Mach	$V_\infty, m/s$	$\rho_\infty, kg/m^3$	T_∞, K	CA	CN	Cm
0.0	2.09	472	4.634E-03	190.2	1.368d+00	0.000d-00	0.000d-00
0.0	3.00	679	3.834E-03	189.9	1.475d+00	0.000d-00	0.000d-00
0.0	3.95	892	*3.834E-03*	189.9	1.531d+00	0.000d-00	0.000d-00
0.0	4.82	1089	3.802E-03	189.7	1.563d+00	0.000d-00	0.000d-00
0.0	5.83	1317	3.776E-03	189.6	1.588d+00	0.000d-00	0.000d-00
6.0	2.09	472	4.634E-03	190.2	1.359d+00	1.460d-02	-1.415d-02
6.0	3.00	679	3.834E-03	189.9	1.464d+00	1.478d-02	-1.416d-02
6.0	3.95	892	3.834E-03	189.9	1.519d+00	1.455d-02	-1.373d-02
6.0	4.82	1089	3.802E-03	189.7	1.551d+00	1.409d-02	-1.305d-02
6.0	5.83	1317	3.776E-03	189.6	1.576d+00	1.362d-02	-1.238d-02
11.0	2.09	472	4.634E-03	190.2	1.337d+00	2.667d-02	-2.579d-02
11.0	3.00	679	3.834E-03	189.9	1.439d+00	2.701d-02	-2.577d-02
11.0	3.95	892	3.834E-03	189.9	1.490d+00	2.672d-02	-2.503d-02
11.0	4.82	1089	3.802E-03	189.7	1.518d+00	2.626d-02	-2.413d-02
11.0	5.83	1317	3.776E-03	189.6	1.538d+00	2.609d-02	-2.350d-02
16.0	2.09	472	4.634E-03	190.2	1.302d+00	3.868d-02	-3.726d-02
16.0	3.00	679	3.834E-03	189.9	1.395d+00	3.953d-02	-3.748d-02
16.0	3.95	892	3.834E-03	189.9	1.436d+00	4.035d-02	-3.751d-02
16.0	4.82	1089	3.802E-03	189.7	1.454d+00	4.185d-02	-3.839d-02
16.0	5.83	1317	3.776E-03	189.6	1.464d+00	4.373d-02	-3.985d-02
20.0	2.09	472	4.634E-03	190.2	1.264d+00	4.836d-02	-4.637d-02
20.0	3.00	679	3.834E-03	189.9	1.344d+00	5.053d-02	-4.761d-02
20.0	3.95	892	3.834E-03	189.9	1.371d+00	5.390d-02	-5.002d-02
20.0	4.82	1089	3.802E-03	189.7	1.383d+00	5.693d-02	-5.250d-02
20.0	5.83	1317	3.776E-03	189.6	1.391d+00	5.959d-02	-5.479d-02
24.0	2.09	472	4.634E-03	190.2	1.215d+00	5.829d-02	-5.554d-02
24.0	3.00	679	3.834E-03	189.9	1.277d+00	6.314d-02	-5.919d-02
24.0	3.95	892	3.834E-03	189.9	1.295d+00	6.892d-02	-6.404d-02
24.0	4.82	1089	3.802E-03	189.7	1.303d+00	7.273d-02	-6.736d-02
24.0	5.83	1317	3.776E-03	189.6	1.309d+00	7.578d-02	-7.009d-02

Table 5. Hypersonic forebody LAURA data, MRP X/D = 0.2498, Z/D = 0.0

α_{total}	Mach	$V_\infty, m/s$	$\rho_\infty, kg/m^3$	T_∞, K	CA	CN	Cm
14.0	8.86	2000	3.483E-03	189.4	1.513d+00	3.933d-02	-2.554d-02
14.0	10.63	2400	3.168E-03	189.4	1.518d+00	4.044d-02	-2.624d-02
14.0	16.06	3600	1.926E-03	186.8	1.536d+00	4.466d-02	-2.912d-02
14.0	17.00	3800	1.723E-03	185.8	1.538d+00	4.533d-02	-2.959d-02
14.0	17.98	4000	1.517E-03	184.0	1.539d+00	4.588d-02	-2.997d-02
14.0	18.98	4200	1.312E-03	182.0	1.539d+00	4.634d-02	-3.027d-02
14.0	20.01	4400	1.117E-03	179.8	1.540d+00	4.673d-02	-3.052d-02
14.0	21.11	4600	9.331E-04	176.4	1.540d+00	4.704d-02	-3.070d-02
14.0	22.31	4800	7.430E-04	172.1	1.540d+00	4.729d-02	-3.081d-02
14.0	23.66	5000	5.520E-04	166.0	1.539d+00	4.749d-02	-3.088d-02
14.0	25.27	5200	3.448E-04	157.3	1.538d+00	4.761d-02	-3.072d-02
14.0	27.21	5400	1.153E-04	146.4	1.537d+00	4.826d-02	-3.014d-02
16.0	8.86	2000	3.483E-03	189.4	1.478d+00	4.744d-02	-3.121d-02
16.0	10.63	2400	3.168E-03	189.4	1.482d+00	4.862d-02	-3.199d-02
16.0	16.06	3600	1.926E-03	186.8	1.500d+00	5.271d-02	-3.486d-02
16.0	17.00	3800	1.723E-03	185.8	1.501d+00	5.336d-02	-3.533d-02
16.0	17.98	4000	1.517E-03	184.0	1.502d+00	5.390d-02	-3.571d-02
16.0	18.98	4200	1.312E-03	182.0	1.503d+00	5.436d-02	-3.601d-02
16.0	20.01	4400	1.117E-03	179.8	1.503d+00	5.476d-02	-3.627d-02
16.0	21.11	4600	9.331E-04	176.4	1.503d+00	5.507d-02	-3.648d-02
16.0	22.31	4800	7.430E-04	172.1	1.243d+00	1.361d-01	-1.134d-01
16.0	23.66	5000	5.520E-04	166.0	1.502d+00	5.554d-02	-3.666d-02
16.0	25.27	5200	3.448E-04	157.3	1.501d+00	5.575d-02	-3.659d-02
16.0	27.21	5400	1.153E-04	146.4	1.500d+00	5.648d-02	-3.610d-02
17.0	8.86	2000	3.483E-03	189.4	1.460d+00	5.153d-02	-3.408d-02
17.0	10.63	2400	3.168E-03	189.4	1.464d+00	5.275d-02	-3.488d-02
17.0	16.06	3600	1.926E-03	186.8	1.482d+00	5.677d-02	-3.775d-02
17.0	17.00	3800	1.723E-03	185.8	1.483d+00	5.742d-02	-3.822d-02
17.0	17.98	4000	1.517E-03	184.0	1.483d+00	5.797d-02	-3.860d-02
17.0	18.98	4200	1.312E-03	182.0	1.484d+00	5.844d-02	-3.893d-02
17.0	20.01	4400	1.117E-03	179.8	1.484d+00	5.879d-02	-3.915d-02
17.0	21.11	4600	9.331E-04	176.4	1.484d+00	5.916d-02	-3.938d-02
17.0	22.31	4800	7.430E-04	172.1	1.483d+00	5.943d-02	-3.953d-02
17.0	23.66	5000	5.520E-04	166.0	1.483d+00	5.965d-02	-3.961d-02
17.0	25.27	5200	3.448E-04	157.3	1.482d+00	5.987d-02	-3.954d-02
17.0	27.21	5400	1.153E-04	146.4	1.481d+00	6.062d-02	-3.905d-02
18.0	10.63	2400	3.168E-03	189.4	1.444d+00	5.689d-02	-3.778d-02
18.0	16.06	3600	1.926E-03	186.8	1.462d+00	6.085d-02	-4.062d-02
18.0	17.00	3800	1.723E-03	185.8	1.463d+00	6.150d-02	-4.110d-02
18.0	17.98	4000	1.517E-03	184.0	1.464d+00	6.204d-02	-4.148d-02
18.0	18.98	4200	1.312E-03	182.0	1.464d+00	6.251d-02	-4.181d-02
18.0	20.01	4400	1.117E-03	179.8	1.464d+00	6.291d-02	-4.207d-02
18.0	21.11	4600	9.331E-04	176.4	1.464d+00	6.325d-02	-4.229d-02
18.0	22.31	4800	7.430E-04	172.1	1.464d+00	6.353d-02	-4.244d-02
18.0	23.66	5000	5.520E-04	166.0	1.463d+00	6.373d-02	-4.249d-02
18.0	25.27	5200	3.448E-04	157.3	1.462d+00	6.399d-02	-4.245d-02
18.0	27.21	5400	1.153E-04	146.4	1.461d+00	6.479d-02	-4.201d-02

Table 6. Hypersonic forebody LAURA data (continued from previous page)

α_{total}	Mach	$V_\infty, m/s$	$\rho_\infty, kg/m^3$	T_∞, K	CA	CN	Cm
20.0	8.86	2000	3.483E-03	189.4	1.402d+00	6.385d-02	-4.268d-02
20.0	10.63	2400	3.168E-03	189.4	1.405d+00	6.517d-02	-4.356d-02
20.0	16.06	3600	1.926E-03	186.8	1.422d+00	6.904d-02	-4.636d-02
20.0	17.00	3800	1.723E-03	185.8	1.423d+00	6.968d-02	-4.684d-02
20.0	17.98	4000	1.517E-03	184.0	1.423d+00	7.022d-02	-4.723d-02
20.0	18.98	4200	1.312E-03	182.0	1.424d+00	7.067d-02	-4.754d-02
20.0	20.01	4400	1.117E-03	179.8	1.424d+00	7.107d-02	-4.781d-02
20.0	21.11	4600	9.331E-04	176.4	1.424d+00	7.143d-02	-4.803d-02
20.0	22.31	4800	7.430E-04	172.1	1.423d+00	7.173d-02	-4.821d-02
20.0	23.66	5000	5.520E-04	166.0	1.423d+00	7.194d-02	-4.825d-02
20.0	25.27	5200	3.448E-04	157.3	1.422d+00	7.225d-02	-4.824d-02
20.0	27.21	5400	1.153E-04	146.4	1.420d+00	7.319d-02	-4.787d-02
24.0	8.86	2000	3.483E-03	189.4	1.318d+00	8.033d-02	-5.412d-02
24.0	10.63	2400	3.168E-03	189.4	1.320d+00	8.168d-02	-5.501d-02
24.0	16.06	3600	1.926E-03	186.8	1.337d+00	8.542d-02	-5.760d-02
24.0	17.00	3800	1.723E-03	185.8	1.338d+00	8.597d-02	-5.803d-02
24.0	17.98	4000	1.517E-03	184.0	1.339d+00	8.651d-02	-5.843d-02
24.0	18.98	4200	1.312E-03	182.0	1.339d+00	8.699d-02	-5.877d-02
24.0	20.01	4400	1.117E-03	179.8	1.339d+00	8.743d-02	-5.909d-02
24.0	21.11	4600	9.331E-04	176.4	1.338d+00	8.778d-02	-5.933d-02
24.0	22.31	4800	7.430E-04	172.1	1.338d+00	8.814d-02	-5.953d-02
24.0	23.66	5000	5.520E-04	166.0	1.337d+00	8.836d-02	-5.956d-02
24.0	25.27	5200	3.448E-04	157.3	1.336d+00	8.871d-02	-5.953d-02
24.0	27.21	5400	1.153E-04	146.4	1.334d+00	8.990d-02	-5.922d-02

American Institute of Aeronautics and Astronautics